PHYSICAL REVIEW B VOLUME 37, NUMBER 16 1 JUNE 1988

Excited-state absorption of Ni^{2+} in MgF_2 and MgO

R. Moncorgé and T. Benyattou

Laboratoire de Physico-Chimie des Matériaux Luminescents, Université de Lyon I,
43 boulevard du 11 Novembre 1918, 69622 Villeurbanne, France

(Received 6 July 1987; revised manuscript received 9 October 1987)

We report an analysis of the excited-state dynamics, fluorescence, as well as excited-state absorption, in the Ni^{2+}-doped vibronic laser systems $MgO:Ni^{2+}$ and $MgF_2:Ni^{2+}$. Use is made of this analysis to show the ability and the limitations of the single-configuration-coordinate model and the Struck and Fonger theory to describe or predict the gross features of the ground-state and the excited-state absorption and emission data.

I. INTRODUCTION

There is now a renewed and increased interest in the search and the development of the vibronic solid-state laser systems based on phonon-terminated optical transitions of transition-metal ions in fluoride and oxide hosts as stable and tunable light sources for spectroscopy as well as high-power lasers. This interest is shown through the number of papers which have been published on the subject in the last few years and through the recently created conference on tunable solid-state lasers. However, though many systems have been discovered and operated successfully as tunable lasers, we still note a lack of realistic models and spectroscopic data allowing us to predict or even fully understand the lasing properties.

For example, an underdeveloped area in the optical spectroscopy of the fluorescent transition-metal ions is excited-state absorption (ESA). In the lasing wavelength region, this absorption often competes with the stimulated emission and decreases the laser output; in the pump region, it causes losses of energy from the pump light into heat or converts the pump light into undesired fluorescence. Consequently, we must know as much about ESA as we know about the radiative and nonradiative processes or the mechanical and thermal properties of the materials.

There have been several reports on the ESA of Cr^{3+} in high-field systems, such as ruby, emerald, $MgO:Cr^{3+}$, and alexandrite;[1,2] the ESA transitions are attributed there to electronic transitions of the type $^2E \rightarrow$ higher states. This has been completed very recently by Andrews *et al.*[3] with a study of the ESA of Cr^{3+} in low-field systems, K_2NaScF_6, $Gd_3(Sc,Ga)_2Ga_3O_{12}$ (GSGG), $Gd_3Sc_2Al_3O_{12}$ (GSAG), in which the ESA electronic transitions are of the type $^4T_{2g} \rightarrow$ higher states.

No study has appeared so far on the ESA of the V^{2+}, Co^{2+}, or Ni^{2+} ions in fluorides or oxides, though ESA is known to be particularly detrimental for laser action in many of these systems.

This paper is devoted to an analysis of the excited-state dynamics (fluorescence as well as excited-state absorption) in the Ni^{2+}-doped compounds MgF_2 and MgO, two laser hosts having rather different structural properties. It follows an analysis on the ESA of V^{2+} in MgF_2 and $KMgF_3$.[4]

Our main purpose is to give fundamental information, to assess, for example, up to what extent a single configuration coordinate model is valid for predicting the various features of the ground-state as well as excited-state optical transitions.

The paper is divided as follows. Section II is devoted to the description of the materials and experimental techniques. The general spectroscopic data are gathered in Sec. III. The excited-state excitation and absorption spectra are described in Secs. IV and V. The data are compared with the predictions of the single configuration coordinate model and discussed in Sec. VI.

II. MATERIALS AND TECHNIQUES

The excited-state excitation and the fluorescence spectra are obtained by exciting the samples with a powerful Nd^{3+}-doped $(Y_3Al_5O_{12})$ (YAG) pumped dye laser from Quantel (Datachrom model) which delivers excitation pulses of 15 ns duration and 0.1 cm^{-1} spectral width. The dyes used for exciting in the visible domain are Rhodamines from Exciton, R590, R610, R640 and mixtures of them, R590 + R610, R610 + R640 for wavelengths between 545 and 625 nm and also other Exciton dyes called DCM and LD700 and mixtures of them, DCM + LD700 for wavelengths between 620 and 745 nm. The infrared excitations are produced with the help of a very efficient hydrogen Raman cell which shifts the energy of the dye laser beam going through it by -4155 cm^{-1} (Stokes 1) and -2×4155 cm^{-1} (Stokes 2). The intensity fluctuations at the output of the cell are $\sim 10\%$ for the Stokes 1 and $\sim 20\%$ for the Stokes 2 shifted radiations. By this way, excitation pulses of a few millijoules can be obtained up to wavelengths of ~ 1.95 μm.

Fluorescence has been analyzed with the aid of a 1-m Jobin-Yvon HRS1 monochromator with a grating of 1200 grooves/mm and blazed at 500 nm for the visible or a Bausch-Lomb model IR No. 1 monochromator with a grating of 675 grooves/mm and blazed at 1 μm for the infrared. Fluorescence up to 1 μm is detected by fast response photomultipliers (9789 EMI, 9808 EMI) and the signals are fed either into an Ortec photon-counting system which is connected to a calculator for the spectral measurements or an IN90 Inter-Technique multichannel analyzer for the lifetime data. In the range 1.0–1.7 μm, fluorescence is detected by an ADC model 403 HS germanium photodiode cooled to liquid-nitrogen (LN) temperature, with a time response of about 200 ns, and the signals are fed into a PAR model 162/165 boxcar averager interfaced with the calculator or a Hewlett-Packard model 19860 A sampling oscilloscope.

III. GENERAL SPECTROSCOPIC DATA

The absorption and emission spectra of $MgF_2{:}Ni^{2+}$ and $MgO{:}Ni^{2+}$ at low temperature are shown in Figs. 1 and 2. They are made of sharp lines superimposed on broadbands, in the visible as well as in the infrared regions, characteristic of zero-phonon electronic transitions, phonon satellites, and vibronic sidebands in the Ni^{2+} ions; it is precisely the broad vibronic sidebands which allow pumping by available sources—some of them are indicated on the left-hand side of the figures—and tunable four-level operation. The various features are labeled in both systems according to the notations on the irreducible representations of the group of octahedral symmetry and, as much as possible, according to the notations associated to the perturbating effects such as local field distortion (case MgF_2) and spin-orbit coupling (case of MgO).

The absorption spectra are characterized by three spin-allowed and two spin-forbidden optical transitions. The transitions to the singlet state ^1E and $^1T_2(^1D)$ becomes spin allowed through second-order spin-orbit coupling. Because of the inversion site symmetry, no electric dipole zero-phonon lines can be observed, but the associated phonon satellites and vibronic sidebands relative to the $^3T_1(^3F)$, $^1T_2(^1D)$, and $^3T_1(^3P)$ excited states are electric dipole in nature: they are forced electric dipole transitions induced by interactions with odd-parity phonon modes of T_{1u} symmetry. It is difficult to say much from the spectral shape of the band relative to the $^1E(^1D)$ excited state, since it is weak and overlaps too much with the $^3T_1(^3F)$ band.

The electronic transition to the lowest triplet state $^3T_2(^3F)$ is the only magnetic-dipole-allowed transition; one observes indeed, very sharp magnetic dipole zero-

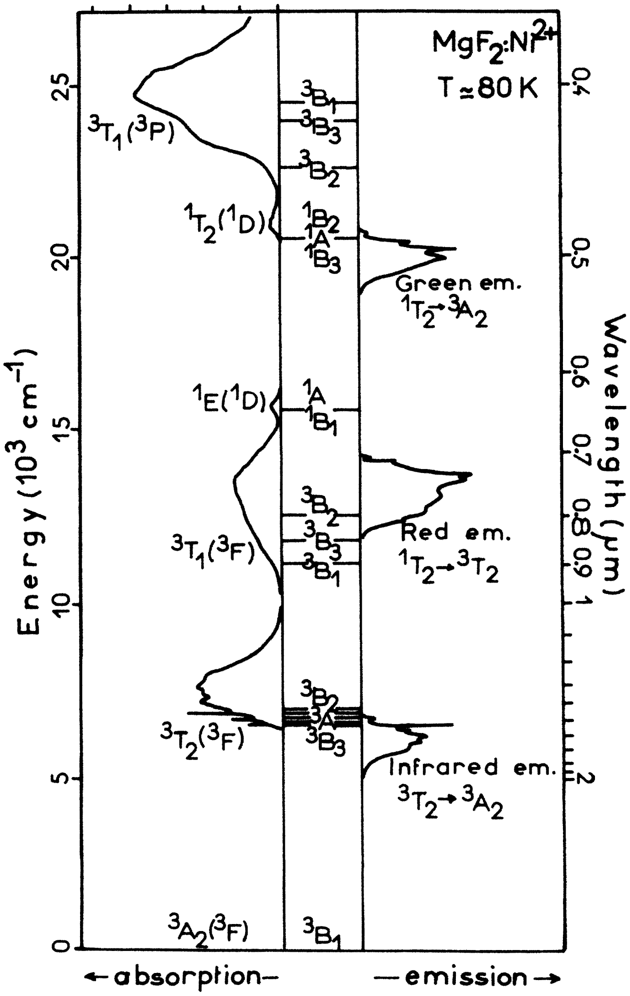

FIG. 1. Low-temperature emission (right-hand side) and absorption spectra (left-hand side) and estimated positions of the zero-phonon orbital components (center) of the energy levels in $MgF_2{:}Ni^{2+}$.

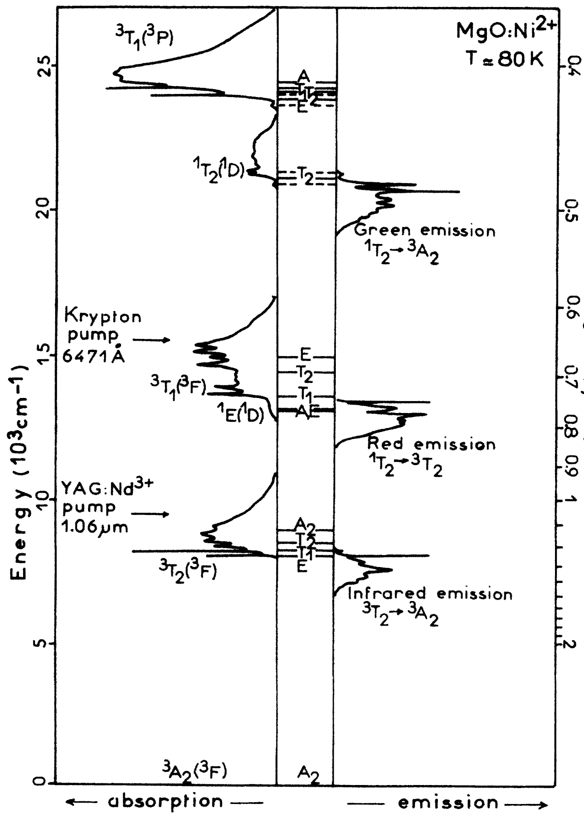

FIG. 2. Low-temperature emission (right-hand side) and absorption spectra (left-hand side) and estimated positions of the zero-phonon spin-orbit components (center) of energy levels in $MgO{:}Ni^{2+}$.

phonon lines but also, vibronic sidebands with a major magnetic dipole character.

The emission spectra also consist of sharp no-phonon lines and phonon satellites and broad vibronic sidebands; they correspond to three downward electronic transitions, two of them, in the green and red spectral domains, originating from the $^1T_2(^1D)$ excited state, a third one, which is essential for infrared laser action, coming from the lowest excited state $^3T_2(^3F)$.

In the case of MgO:Ni^{2+} the sideband structures are made principally from double peaked phonon satellites of the various spin-orbit components at $\sim$200 and 400 cm^{-1} due to T_{1u} excitations.[5-11] Evidence is also found in the $^3T_2(^3F)$ (Ref. 12) and $^1T_2(^1D)$ (Ref. 13) states, of interacting phonons of E_g symmetry, leading to a non-negligible Jahn-Teller (JT) effect with a 515 cm^1 JT energy in the case of $^1T_2(^1D)$ state. Also, using the data provided by the temperature dependences of the bandwidths,[5] a ground-state mean-phonon frequency of about 310 cm^{-1} can be found. Considering the fluorescence data, a computer program can be used to fit the temperature dependences of the ir and green (or red) emission lifetimes to the expression of the theory of Struck and Fonger (SF):

$$\frac{1}{\tau}=\frac{1}{\tau_0}+N_u U_{P_u} ,$$

where τ_0 is the radiation lifetime, N_u a constant of the model and U_{P_u} the summed Franck-Condon (FC) weight defined in the SF theory. U_{P_u} depends on P_u and $\hbar\omega$, the number and the mean energy of the interacting phonon needed to overcome the transition gap, and on S, the Huang-Rhys factor. Treating the latter as parameters, one obtains the following values.

For the infrared lifetime[11] $S=3.38$, $P_u=26$, and $\hbar\omega=308$ cm^{-1} with $N_u=1\times10^{13}$ and $\tau_0=3.6$ ms, the low-temperature fluoresence lifetime.

For the green (or red) lifetime $S=2.56$, $P_u=19$, and $\hbar\omega=255$ cm^{-1}, with $N_u=1\times10^{13}$ and $\tau_0=1.2$ ms.

In the case of MgF_2:Ni^{2+}, the local field distortion and the spin-orbit coupling make the band structures more difficult to analyze. Except for the infrared level $^3T_2(^3F)$, for which a number of magnetic dipole zero-phonon lines associated with various spin-orbit components can be clearly identified,[14] the other levels are treated only by considering the effect of the orthorhombic crystal field on the orbital components which is far from being satisfactory, particularly in the case of the triplet states $^3T_1(^3F)$ and $^3T_1(^3P)$.

If one uses the data provided by the temperature dependences of the absorption and of the emission bandwidths, ground state, and first excited-state mean-phonon frequencies of about 410 and 155 cm^{-1} can be found in good agreement with characteristic peaks in the phonon density of states[15] of MgF_2:Ni^{2+}. The fitting of the Struck and Fonger model to the decay data give in turn, the parameter values.[16]

For the infrared lifetime, $S=3.24$, $P_u=26$, $\hbar\omega=250$ cm^{-1}, $N_u=1\times10^{13}$, and $\tau_0=12$ ms.

For the green (or red) lifetime, $S=2.56$, $P_u=19$, $\hbar\omega=250$ cm^{-1}, $N_u=1\times10^{13}$, and $\tau_0=430$ μs.

In the case of MgO:Ni^{2+} as well as MgF_2:Ni^{2+}, the fits of the Struck and Fonger model to the infrared decay data give products $P_u\hbar\omega=6500$ and 8008 cm^{-1} which agree fairly well with the respective zero-phonon energies that one finds experimentally.

The parameter values obtained with the green (or red) fluorescence decay data are more questionable. In MgF_2:Ni^{2+}, the lifetime τ_0 corresponds well to the low-temperature measured lifetime of the emitting level, but this lifetime value is short with respect to the expected lifetime calculated from the absorption data; also, as already asserted, it must include a non-negligible nonradiative component even at the lowest temperatures. On the other hand, the product $P_u\hbar\omega$ gives 4750 cm^{-1}, a value which is fairly close to the energy gap between the zero-phonon levels of the states $^1T_2(^1D)$ and $^1E(^1D)$ at $\sim$20 530 and 15 500 cm^{-1}, thus indicating the most likely nonradiative decay channel for the green (or red) fluorescence. In MgO:Ni^{2+}, the $^1E(^1D)$ state stands below the $^3T_1(^3F)$ state and a different decay channel could be invoked: it manifests itself in the parameter value obtained for $\tau_0=1.2$ ms since it agrees better with the value calculated from the absorption data; on the other hand, the product $P\hbar\omega$ gives 4335 cm^{-1}, a value which is now very different from the energy gap of $\sim$8100 cm^{-1} between the states $^1T_2(^1D)$ and $^1E(^1D)$ or the energy gap of $\sim$6100 cm^{-1} which is estimated between the state $^1T_2(^1D)$ and the higher-energy spin-orbit (SO) component of the state $^3T_1(^3F)$. One might wonder instead if the main nonradiative deexcitation process of the state $^1T_2(^1D)$ could take place via the upper state $^3T_1(^3P)$, which then could apply in the case of MgF_2:Ni^{2+} as well as in MgO:Ni^{2+}.

TABLE I. Laser data on the Ni^{2+}-doped MgF_2 and MgO vibronic systems.

Laser system	Lifetime at 80 K (ms)	Emission cross section (cm^2)	Wavelength of YAG:Nd^{3+} pump source (μm)	Slope quant. efficiency (%)	TEM_{00} max output power (W)	Tuning range (μm)
MgO:Ni^{2+} (Refs. 20,21)	3.6	1.6×10^{-21}	1.06	57	10	1.316–1.409
MgF_2:Ni^{2+} (Refs. 19,20)	13	5×10^{-21}	1.32	37	2	1.61 –1.74

The different energy level spacing in MgF_2:Ni^{2+} and MgO:Ni^{2+} also lead to the following observations. In MgF_2:Ni^{2+}, we have observed coincidences between the energy of the $^1T_2(^1D)\rightarrow{}^3T_2(^3F)$ red emission transition, the energy of excitation of the vibronic sideband associated with the $^3A_2(^3F)\rightarrow{}^3T_1(^3F)$ transition and the excited-state absorption energy $^3T_1(^3F)\rightarrow{}^3T_1(^3P)$. The former coincidence gives rise to a cross relaxation type energy transfer process which strongly affects the green (or red) fluorescence dynamics.[17] The coincidence between the last two energies gives rise to very detrimental losses for infrared laser action when the system is pumped for example with the continuous-wave (cw) radiation at 7525 Å of a krypton laser.[17]

In MgO:Ni^{2+} there are no such coincidences. As a consequence, the emitting level $^1T_2(^1D)$ is not subject to any energy transfer process [the decay mode of the associated green (or red) fluorescence remains exponential] and no excited-state absorption of type $^3T_1(^3F)\rightarrow{}^3T_1(^3P)$ should occur if one pumps for example with the 6471 Å radiation of a cw Krypton laser, which does not mean that no excited-state absorption will occur at this energy (see the following section).

We have reported in Table I the most important data concerning the infrared laser emission of each laser material. In both cases the estimated emission cross section is of the same order of magnitude. The systems differ in their optimum pump wavelength, their laser internal quantum efficiency (the ratio of the number of stimulated photons to the number of absorbed pump photons), the maximum output power which has been already obtained, and their range of wavelength tunability.[17–21] These data are given for $T \simeq 77$ K, the temperature at which the two lasers have been working. However, cw operation of MgO:Ni^{2+} has been demonstrated up to −30 °C and the authors thought that pulsed operation would be straightforward at room temperature;[20] it is due to the weakness of the nonradiative transitions from the $^3T_2(^3F)$ infrared emitting level to the ground state in this range of temperature, which manifests itself in the slow variation of the associated fluorescence lifetime. As an introductory remark for the following section, we can already note that the laser internal quantum efficiency is less than unity and, as it has been already noted a number of times in the past, this reduction must be related to the existence of excited-state absorption in the wavelength domain of the pump radiation as well as in the domain of laser emission.

TABLE II. Observed and estimated positions of the orthorhombic components of the zero-phonon electronic energy levels in MgF_2:Ni^{2+} and associated Huang-Rhys factor S.

Excited levels (orthorhombic components)	Zero-phonon energy (cm^{-1})	S parameter
$^3T_2(^3F)\,^3B_3$	6 506	1.38
	6 541	
^3A	6 636	
	6 672	
$^3B_2$	6 797	
	6 920	
	(after Ref. 14)	
$^3T_1(^3F)\,^3B_1$	11 200±100	~3.45
$^3B_3$	11 800±100	
$^3B_2$	12 600±100	
$^1E(^1D)\,^1A$		~0
	~15 500	
$^1B_1$		
$^1T_2(^1D)^1B_3$		1.73
^1A	20 535	
$^1B_2$		
$^3T_1(^3P)\,^3B_1$	22 700±100	~2.74
$^3B_2$	24 000±100	
$^3B_3$	24 500±100	

IV. EXCITED-STATE EXCITATION (ESE) SPECTRA

A. MgF_2:Ni^{2+}

We have shown in a previous paper[17] that a bright green anti-Stokes fluoresence can be observed in MgF_2:Ni^{2+} when the crystal is excited by the 7525 Å radiation of a krypton-pump laser, i.e., in the $^3T_1(^3F)$ absorption band. This anti-Stokes emission has been attributed to the green emission located around 5000 Å associated with the $^1T_2(^1D)\rightarrow{}^3A_2(^3F)$ characteristic transition of the Ni^{2+} ion in this material and we have assumed that excited-state absorption from state $^3T_1(^3F)$ to state $^3T_1(^3P)$ followed by phonon relaxation between states $^3T_1(^3P)$ and $^1T_2(^1D)$ should be responsible for that. It is the first time we have to assume an excited-state absorption from a state located above the lowest metastable excited state.

We have proved that by pumping the crystal at low temperature in the whole wavelength domain of the $^3A_2(^3F)\rightarrow{}^3T_1(^3F)$ absorption band and by monitoring the resulting green anti-Stokes fluorescence. We have used as many as five different dyes. The excited-state excitation spectra are reported on Figs. 3–5; they have been corrected from the dye laser intensities but they have not from the $^3A_2(^3F)\rightarrow{}^3T_1(^3F)$ absorption band shape because it is not necessary for the assignments.

Indeed, just by looking at the positions of the energy levels of the Ni^{2+} ion in MgF_2, as reported in Fig. 1, energetic considerations alone make the following assignments possible: (1) the 715–890 nm spectral region to a $^3T_1(^3F)\rightarrow{}^3T_1(^3P)$ excited-state absorption in agreement with the assumption made before (see Figs. 3 and 4); (2) the 640–715 nm spectral region to a $^3T_2(^3F)\rightarrow{}^1T_2(^1D)$ ESA (see Fig. 4); (3) the 620–630 nm spectra region to the beginning of the $^3T_2(^3F)\rightarrow{}^3T_1(^3P)$ ESA (see Fig. 5). These spectra allow us to make a number of observations.

Because of the weak intensity of the $^3A_2(^3F)\rightarrow[^3T_1(^3F),\ ^1E(^1D)]$ absorption band between 620 and

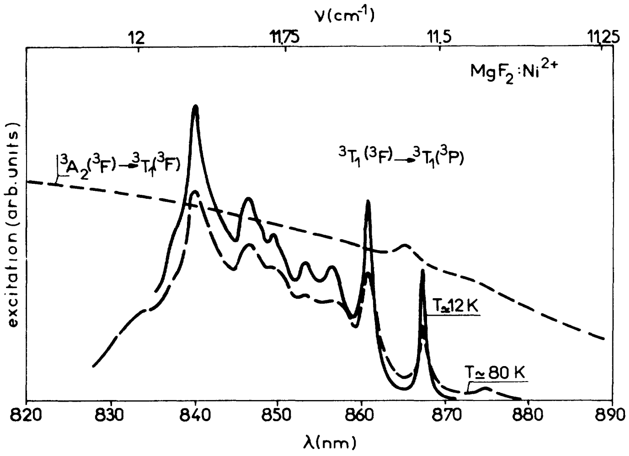

FIG. 3. ${}^3T_1({}^3F)\rightarrow{}^3T_1({}^3P)$ ESE (——) and ${}^3A_2({}^3F)\rightarrow{}^1T_1({}^3F)$ GSA spectra (— — —) of MgF$_2$:Ni^{2+} at low temperature.

630 nm, it may be that the ${}^3T_2({}^3F)\rightarrow{}^3T_1({}^3P)$ ESA transition is more intense than the other two. Also, both the ${}^3T_1({}^3F)\rightarrow{}^3T_1({}^3P)$ and the ${}^3T_2({}^3F)\rightarrow{}^1T_2({}^1D)$ excited-state excitation spectra are made of broadbands as well as sharp structures which indicate that the potential curves corresponding to each state are non-negligibly displaced between each other.

This information is not accessible through the ground-state absorption (GSA) spectra. However, it could be expected in the case of the ${}^3T_2({}^3F)\rightarrow{}^1T_2({}^1D)$ transition since the red emission which corresponds to the reverse process ${}^1T_2({}^1D)\rightarrow{}^3T_2({}^3F)$ also consists of a broadband.

The sharp structures must be related to some magnetic-dipole-allowed zero-phonon transitions or phonon satellites and complementary information can be derived concerning the positions of the various electronic levels and the energies of the active phonon modes. It is clear, for example, that the sharp lines located at about 707.8 nm (14 127 cm^{-1}) and 710.5 nm (14 074 cm^{-1}) separated by ~53 cm^{-1} must be attributed to magnetic-dipole-allowed transitions from the lowest spin-orbit component of the ${}^3T_2({}^3B_3)$ state to the two lowest orthorhombic components of the ${}^1T_2({}^1D)$ singlet state, ${}^3T_2(B_1)\rightarrow{}^1T_2({}^1B_3)$, ${}^1T_2({}^1A)$.

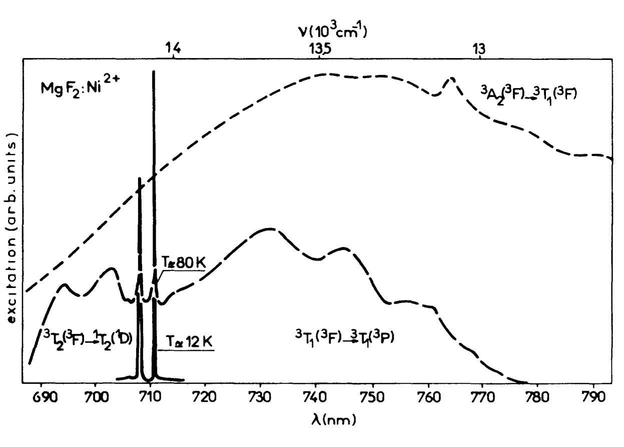

FIG. 4. ${}^3T_2({}^3F)\rightarrow{}^1T_2({}^1D)$ and ${}^3T_1({}^3F)\rightarrow{}^3T_1({}^3P)$ ESE (——) and ${}^3A_2({}^3F)\rightarrow{}^3T_1({}^3F)$ GSA spectra (— — —) of MgF$_2$:Ni^{2+} at $T\simeq80$ K (the portion of the ESE spectrum recorded at $T\simeq12$ K between 705 and 715 nm is shown on a different scale: it is reduced at least by a factor 10).

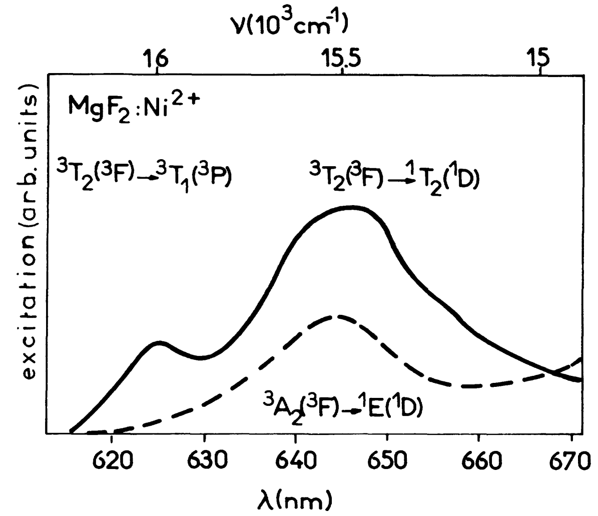

FIG. 5. ${}^3T_2({}^3F)\rightarrow{}^3T_1({}^3P)$ and ${}^3T_2({}^3F)\rightarrow{}^1T_2({}^1D)$ ESE (——) and ${}^3A_2({}^3F)\rightarrow{}^1E({}^1D)$ GSA spectra (— — —) of MgF$_2$:Ni^{2+} at low temperature ($T\simeq80$ K).

The broadbands at about 694 nm (14 409 cm^{-1}) and 703 nm (14 224 cm^{-1}) are attributed to phonon assisted sidebands. Their separations with the 710.5 nm zero-phonon line correlate well with peaks of the MgF$_2$ phonon density of states at 33 and 150 cm^{-1} and phonons of these energies have to be coupled in the ${}^1T_2({}^1D)$ state.

The line structure around 850 nm is even more interesting since we do not know the exact position of the zero-phonon levels of the ${}^3T_1({}^3F)$ and ${}^3T_1({}^3P)$ states participating in this excited-state transition. The shape, the spacing, and the thermal behavior of the various lines allow us to attribute (i) the lines at 867.5 nm (11 527 cm^{-1}) and 861 nm (11 614 cm^{-1}) separated by ~87 cm^{-1} to magnetic-dipole-allowed transitions from the lowest spin-orbit component of the ${}^3T_1({}^3F,{}^3B_1)$ state to the two lowest spin-orbit components of the ${}^3T_1({}^3P,\ {}^3B_2)$, (ii) the double peaked broadbands at ~855 and 848 nm with a common splitting of ~42 cm^{-1}, to two phonon sidebands of the previous lines associated with two characteristic phonon intervals of ~155 and 200 cm^{-1}, and (iii) the line appearing at 80 K around 874.9 nm (11 429 cm^{-1}) to a hot zero-phonon transition from the second spin-orbit component of state ${}^3T_1({}^3F,{}^3B_1)$ to the lowest one of state ${}^3T_1({}^3P,\ {}^3B_2)$, or to a hot phonon satellite of the line at 867.5 or the one at 861 nm with characteristic phonon energies of 98 or 185 cm^{-1}, respectively.

B. MgO:Ni^{2+}

As in MgF$_2$:Ni^{2+}, strong laser excitation in the ${}^3T_1({}^3F)$ excited state in MgO:Ni^{2+} also leads to an excited-state absorption process resulting in the observation of green and red anti-Stokes fluorescences, these two emissions being characteristic of the two downward optical transitions ${}^1T_2({}^1D)\rightarrow{}^3A_2({}^3F)$ and ${}^1T_2({}^1D)\rightarrow{}^3T_2({}^3F)$ in this material.

As above, use is made of these fluorescences to measure the corresponding excited-state excitation spectra at low temperature. However, we have operated differently since we have realized a true two-beam experiment. One laser beam at 1.06 μm is focused onto the crystal to pump the ${}^3T_2({}^3F)$ excited state and another beam, a dye laser beam, is focused colinearly with the former to probe the ${}^1T_2({}^1D)$ and ${}^3T_1({}^3P)$ excited states. The resulting excited-state excitation spectra, corrected for the dye laser intensities, are reported in Figs. 6 and 7. These spectra extend into the same domain as the ${}^3A_2({}^3F)\rightarrow{}^3T_1({}^3F)$ GSA band. However, the excited-state excitation spectra do not need to be corrected further from the intensity of this band since we have used low enough dye laser probe intensities to get no detectable fluorescence signal without pumping with the 1.06 μm radiation.

These spectra can be divided into two parts. One region from 700 to 780 nm is attributed to a ${}^3T_2({}^3F)\rightarrow{}^1T_2({}^1D)$ ESA transition and the other from 560 to 640 nm to a ${}^3T_2({}^3F)\rightarrow{}^3T_1({}^3P)$ ESA transition.

The line at 763 nm (13 106 cm^{-1}) is likely due to a zero-phonon transition starting from the lowest spin-orbit component E of state ${}^3T_2({}^3F)$, i.e., ${}^3T_2({}^3F;E)\rightarrow{}^1T_2({}^1D)$. The one observed at 80 K (and not at 12 K) at 773.5 nm (12 928 cm^{-1}), i.e., at 178 cm^{-1} of the former, an energy equal to the energy splitting of the lowest spin-orbit components E and T_1 of state ${}^3T_2({}^3F)$, is attributed to a hot zero-phonon transition ${}^3T_2({}^3F;T_1)\rightarrow{}^1T_2({}^1D)$. The bands located at about 753.4 nm (13 273 cm^{-1}), 740.5 nm (13 504 cm^{-1}) and 726.8 nm (13 719 cm^{-1}) are attributed to a phonon-sideband progression with energy spacings of 167, 398, and 653 cm^{-1}. In the case of the ${}^3T_2({}^3F)\rightarrow{}^3T_1({}^3P)$ ESE spectral band, the assignments are not so straightforward. Considering the calculated positions and spin-orbit splittings of the energy levels which give the best fit to the ground-state absorption and emission data, we are led to the following assignments (see inset of Fig. 7). (i) The lines observed at 80 K (and not at 12 K) at around 630.9 (15 850 cm^{-1}) and 636.9 nm (15 701 cm^{-1}) are attributed to hot zero-phonon transitions between the T_1 spin-orbit component of state ${}^3T_2({}^3F)$ to the two lowest SO components E and T_2 of state ${}^3T_1({}^3P)$, i.e., ${}^3T_2({}^3F;T_1)\rightarrow{}^3T_1({}^3P,E)$, ${}^3T_1({}^3P,T_2)$. (ii) The line peaking around 623.7 nm (16 033 cm^{-1}) is attributed to the zero-phonon transition ${}^3T_2({}^3F;E)\rightarrow{}^3T_1({}^3P;T_2)$. (iii) The lines at 606.6 nm (16 485 cm^{-1}) and 613.7 nm (16 295 cm^{-1}) to a superposition of phonon sidebands and zero-phonon transitions to the highest SO components T_1 and A_1 of state ${}^3T_1({}^3P)$.

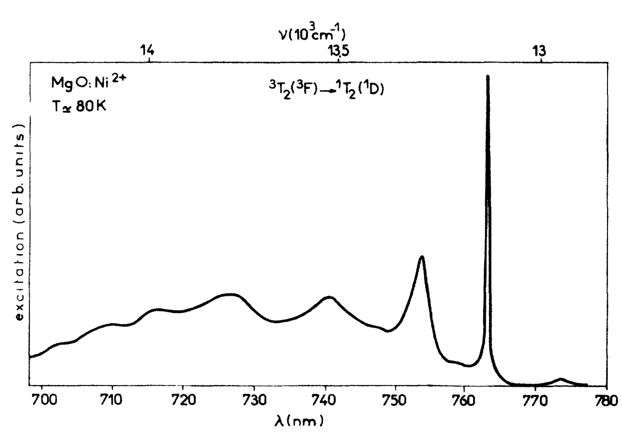

FIG. 6. ${}^3T_2({}^3F)\rightarrow{}^1T_2({}^1D)$ ESE spectrum of MgO:Ni^{2+} at low temperature.

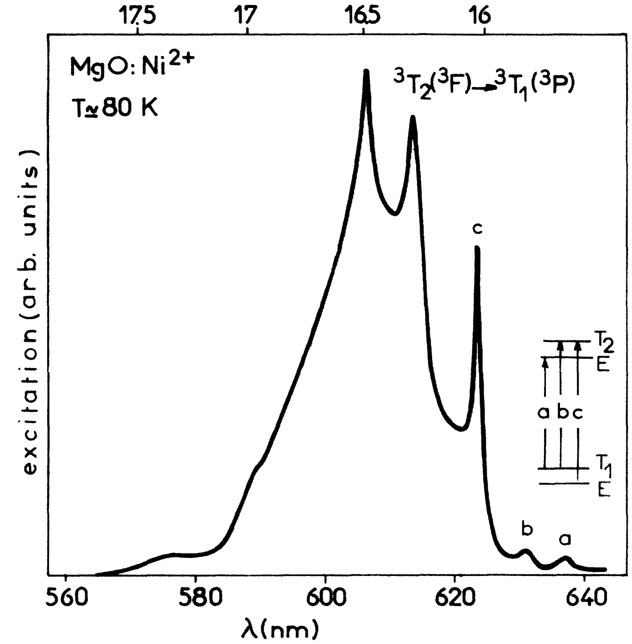

FIG. 7. ${}^3T_2({}^3F)\rightarrow{}^3T_1({}^3P)$ ESE spectrum of MgO:Ni^{2+} at low temperature.

The energy position of the lowest SO component E of state ${}^3T_1({}^3P)$—the above study indicates $\sim$23 890 cm^{-1} (4186 Å)—was further checked in a two-photon excitation experiment. The crystal was pumped with our pulsed dye laser between 800 and 900 nm, i.e., in a wavelength domain where no ground-state absorption occurs (see Fig. 2), and green anti-Stokes fluorescence was detected when we scanned the laser between 820 and 840 nm. The fluorescence intensity increased quadratically with the excitation pump power. This resulted in the two-photon excitation spectrum shown in Fig. 8. It consists of a very sharp line at around 837 nm (11 947 cm^{-1}) which corresponds precisely to the two-photon transition ${}^3A_2\rightarrow{}^3T_1({}^3P,E)$, at $\sim 2\times 11\,947=23\,895$ cm^{-1}, we were looking for. The structure peaking around 829 nm (12 062 cm^{-1}) is attributed in turn to a two-photon phonon sideband ($2\times 12\,062=24\,124$ cm^{-1}) of the latter with a characteristic phonon energy spacing of $\sim$225 cm^{-1}.

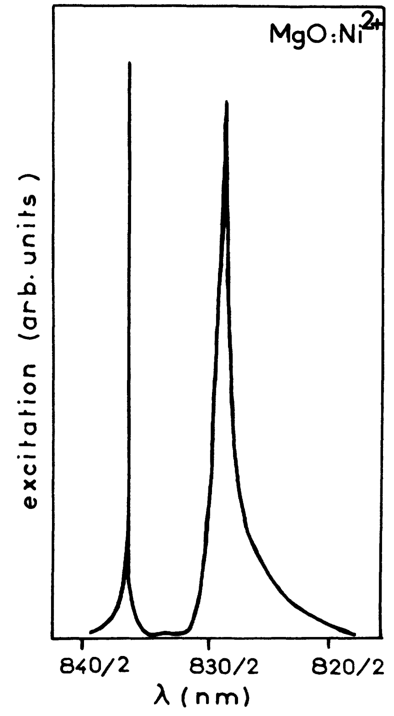

FIG. 8. Two-photon excitation spectrum of MgO:Ni^{2+} at low temperature in the region of the $^3A_2(^3F)\rightarrow{}^3T_1(^3P)$ transition.

No trace of $^3T_1(^3F)\rightarrow{}^3T_1(^3P)$ or $^3T_1(^3F)\rightarrow{}^1T_2(^1D)$ ESA transition is observed and even expected in the spectral domain where these transitions could occur, i.e., in the range between 830 and 1250 nm (8000–12 000 cm^{-1}). We conclude that no ESA process occurs in the $^3T_1(^3F)$ excited state of Ni^{2+} in MgO. This is to be correlated with the respective positions of the $^3T_1(^3F)$ and $^1E(^1D)$ levels in this material. Indeed, in MgO:Ni^{2+}, level $^1E(^1D)$ is at lower energy than level $^3T_1(^3F)$ so that the $^3T_1(^3F)\rightarrow{}^1E(^1D)$ phonon relaxation must be more probable than any excited-state process. Excited-state absorption could occur instead in the $^1E(^1D)$ excited state but we could not check it because of limitations due to the increasing excited-state excitation signal $^3T_2(^3F)\rightarrow{}^3T_1(^3P)$ when the system is pumped in level $^3T_1(^3F)$ and the probe beam is scanned in the expected wavelength domain for the $^1E(^1D)\rightarrow{}^1T_2(^1D)$ transition, i.e., around $\lambda\simeq 1.25$ μm which is precisely the wavelength domain for the ground-state excitation of level $^3T_2(^3F)$.

V. EXCITED-STATE-ABSORPTION CROSS SECTIONS

The excited-state-absorption spectra and cross sections that we are going to describe in this section give us a quantitative view of the importance of ESA mechanisms in these laser materials. The method used to get our ESA spectra is very similar to the one used by Andrews *et al.*,[3] for example, in the case of the Cr^{3+}-doped systems GSGG, GSAG, and K$_2$NaScF$_6$. It consists in the measurement of the change in the transmission (absorption) of a weak probe beam when it passes through a pumped and unpumped crystal. The pump light is provided by the pulsed YAG:Nd^{3+} or the YAG:Nd^{3+} pumped dye laser and the probe by a high power 1 kW halogen lamp source. The transmitted light is analyzed and detected by the monochromators and detectors mentioned in Sec. II. The lenses and pinholes are adjusted to overlap the pump and probe beam in the crystal and to avoid stray light (see Ref. 4).

The spectra are recorded by scanning the monochromator in the wavelength region of interest and by recording and analyzing the transient signal at each selected wavelength.

If I_p and I_u stand for the transmitted probe light intensity when the crystal is pumped and unpumped, respectively, one can write at a particular wavelength

$$I_u = I_0\exp(-\sigma_0 NL) \text{ and } I_p = I_0\exp(-\sigma_1 N_1 L - \sigma_0 N_0 L)\,,$$

where I_0 is the incident light intensity, σ_0 and σ_1 are the absorption cross sections in the ground and excited states labeled (0) and (1), N_0 and N_1 their population densities in the presence of the pump beam knowing that $N_0+N_1=N$ is the total active ion density. L is the light path length in the sample. I_p can be expressed as

$$I_p = I_u\exp-(\sigma_1-\sigma_0)N_1 L\ .$$

Since the excited-state population density N_1 results from a pulsed pump excitation, it transforms like

$$N_1 = N_1(0)\exp-\frac{t}{\tau_1}\ ,$$

where τ_1 is the rate of deexcitation of state (1). When ESA occurs in the metastable state $^3T_2(^3F)$ of Ni^{2+} for example, τ_1 is the lifetime associated with the infrared fluorescence.

As a consequence the observed signal I_p-I_u (I_p-I_u is always much smaller than I_u) is a transient signal which decays approximately with the same time constant as the one characterizing the deexcitation of the absorbing excited state. Dividing I_u by I_p one obtains the change in absorption coefficient $\Delta\alpha$

$$\Delta\alpha = \ln\left[\frac{I_u}{I_p}\right]\Big/L = (\sigma_1-\sigma_0)N_1\ .$$

The time evolution of $\Delta\alpha$ tells us which state is actually absorbing and its zero time value, the value which is retained for the spectra, is directly proportional to the initial excited-state population density $N_1(0)$.

Both σ_0 and N_1 must be known to extract σ_1. σ_0 equals k_0N where k_0 is the ground-state coefficient and N the active ion concentration. N_1 is estimated first from the excitation pump intensity and the pumped volume, then it is checked by comparison with the value obtained from the spectra at the wavelength where $\sigma_1\sim 0$, i.e., $\Delta\alpha=-\sigma_0N_1$. Figures 9 and 10 show both the excited-state difference spectra ($\Delta\alpha$ versus wavelength and/or energy), the GSA spectra, and the resulting ESA of Ni^{2+}-doped MgF$_2$ and MgO at room temperature.

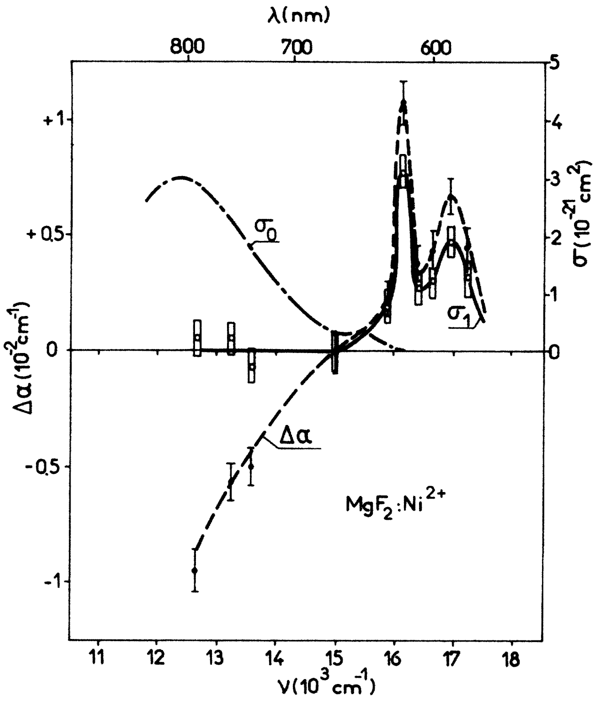

FIG. 9. $A_2(^3F)\rightarrow{}^3T_1(^3P)$ GSA cross section σ_0, measured excited-state difference spectrum $\Delta\alpha$, and ESA cross section σ_1 in MgF_2:Ni^{2+} at room temperature.

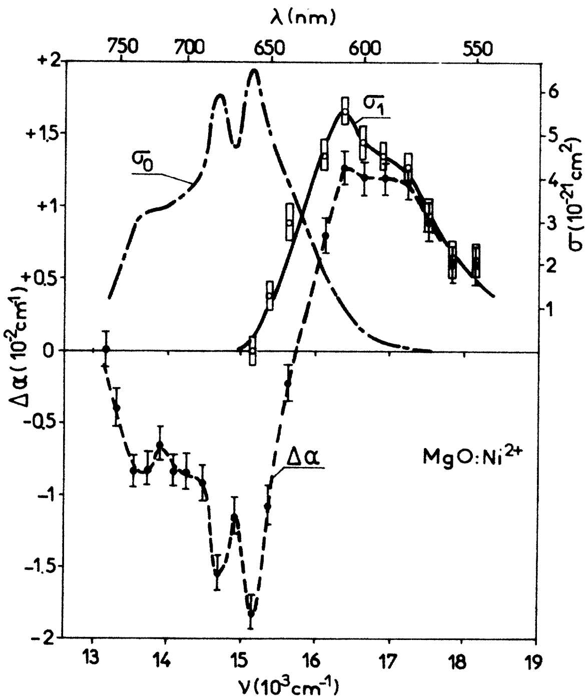

FIG. 10. $^3A_2(^3F)\rightarrow{}^3T_1(^3P)$ GSA cross section σ_0, measured excited-state difference spectrum $\Delta\alpha$, and ESA cross section σ_1 in MgO:Ni^{2+} at room temperature.

The MgF_2:Ni^{2+} single crystal was of high optical quality of 1.66-cm long sample doped with 1.7 at. % Ni^{2+} ions ($N=5.3\times10^{20}$ Ni^{2+} ions/cm^3). The MgO:Ni^{2+} single crystal was a 1.2-cm long sample doped with 0.6 at. % Ni^{2+} ions ($N=3.2\times10^{20}$ Ni^{2+} ions/cm^3). The MgF_2:Ni^{2+} sample was pumped in the $^3T_1(^3F)$ excited state at 7100 Å. The pulsed dye laser beam, with more than 20 mJ per pulse, was focused onto the crystal in order to produce an excited-state population density $N_1\sim(3.5\pm0.8)\times10^{18}$ ions/cm^3. This gives an excitation ratio $N_1/N\sim0.66\%$, which is relatively low. The MgO:Ni^{2+} crystal was pumped directly in the $^3T_2(^3F)$ metastable state of Ni^{2+} with the 1.06 μm radiation of the pulsed YAG:Nd^{3+} laser. More than 30 mJ were focused onto the crystal to create an estimated excited-state population density $N_1\sim(2.8\pm0.6)\times10^{18}$ ions/cm^3, which corresponds to an excitation ratio $N_1/N\sim0.87\%$.

In the case of MgF_2:Ni^{2+} Fig. 9 shows that only the ESA transition $^3T_2(^3F)\rightarrow{}^3T_1(^3P)$ gives rise to a measurable cross section σ_1. In agreement with the ESE spectrum this occurs at wavelengths shorter than $\sim$640 nm ($\nu>15\,500$ cm^{-1}). In the region of the spin-forbidden ESA transition $^3T_2(^3F)\rightarrow{}^1T_2(^1D)$ and of the spin-allowed one $^3T_1(^3F)\rightarrow{}^3T_1(^3P)$, that is at wavelengths between $\sim$640 and 900 nm (11 000 $cm^{-1}<\nu<15\,500$ cm^{-1}), no σ_1 signal can be extracted; in this region, which is also the region of the $^3A_2\rightarrow{}^3T_1(^3F)$ GSA transition with the cross section noted σ_0, only optical pump induced bleaching ($\Delta\alpha<0$) occurs and the excited-state difference spectrum mimics the GSA optical band ($\Delta\alpha=-\sigma_0N_1$).

Because of the spin selection rule, the nonobservation of the $^3T_2(^3F)\rightarrow{}^1T_2(^1D)$ ESA transition is perfectly understandable. A quantitative estimate of the maximum cross section $\sigma_{\max}$ $(^3T_2\rightarrow{}^1T_2)$ can be made starting from the branching ratio of the green $(^1T_2\rightarrow{}^3A_2)$ and red $(^1T_2\rightarrow{}^3T_2)$ emissions observed in this material. The green emission is about 7 times more intense than the red one and they have about the same width at half maximum. Assuming $\sigma_{\max}$ $(^3T_2\rightarrow{}^1T_2)\simeq\sigma_{\max}$ $(^1T_2\rightarrow{}^3T_2)$ one gets, knowing the respective GSA cross sections, $\sigma_{\max}$ $(^3T_2\rightarrow{}^1T_2)\simeq10^{-22}$ cm^2 at $T\simeq80$ K.

Since it does not vary much with temperature—it increases by about a factor 4 between LN and room temperatures (ESE data)—the cross section of this spin-forbidden ESA transition remains much smaller than the spin-allowed one.

Another explanation has to be invoked in the case of the $^3T_1(^3F)\rightarrow{}^3T_1(^3P)$ ESA. Indeed the transient signal corresponding to this type of absorption must be very short lived; it should decay approximately with the same time constant which characterizes the deexcitation process of the $^3T_1(^3F)$ absorbing state. It is likely of a few picoseconds at room temperature, maybe a few nanoseconds at LN temperature. Consequently, the transient signal produced by the $^3T_1(^3F)\rightarrow{}^3T_1(^3P)$ ESA transition, if any signal of this type exists at room temperature, cannot be detected merely because of experimental limitations.

The results are very much similar in the case of MgO:Ni^{2+} (Fig. 10). Only the σ_1 cross section associated with the spin-allowed $^3T_2(^3F)\rightarrow{}^3T_1(^3P)$ ESA transition can be extracted. In agreement with the ESE data, this occurs at wavelengths $\lambda \leq 650$ nm. In the region between 650 and 750 nm ($13\,000\ \mathrm{cm}^{-1} < \nu < 15\,400\ \mathrm{cm}^{-1}$) optical pump induced bleaching takes place ($\Delta\alpha = -\sigma_0 N_1$) and the excited-state difference spectrum $\Delta\alpha$ mimics the GSA optical band σ_0.

Finally, we shall make the two following remarks: (i) the absorption cross sections in these Ni^{2+}-doped compounds are much weaker, about a factor 10, than in the Cr^{3+}-doped systems such as GSGG, GSAG, or K_2NaScF_6,[3] which implies more sensitivity in the pump-probe experiments, and (ii) the cross sections of the spin-allowed ESA and GSA transitions in the same spectral range have about the same order of magnitude which well correlates with the Cr^{3+} results. This seems to be a general result and is further verified in the case of V^{2+} doped compounds.[4]

VI. CONCLUDING REMARKS

Study of the ground-state absorption and emission spectral features, analysis of their thermal characteristics (Sec. III), and comparison with the excited-state-absorption data (Sec. IV) have allowed us to get much information about the positions of the various electronic energy levels—and their associated excited-state phonon energies. These positions are gathered in Tables II and III. Subsequently, we can determine, in the octahedral field approximation, the crystal-field and Racah parameters Dq, B, and C which give, by diagonalizing the well-known Tanabe-Sugano (TS) matrices (including spin-orbit coupling in the case of MgO:Ni^{2+}), the best overall agreement with these estimated zero-phonon energies. It is found $Dq \simeq 665\ \mathrm{cm}^{-1}$, $B \simeq 1000\ \mathrm{cm}^{-1}$, and $C/B \simeq 4.08$ in the case of MgF_2:Ni^{2+}, and $Dq \simeq 831\ \mathrm{cm}^{-1}$, $B \simeq 850\ \mathrm{cm}^{-1}$, $C/B \simeq 4.15$, and $\lambda \simeq 325\ \mathrm{cm}^{-1}$ in the case of MgO:Ni^{2+}. As expected, the Ni^{2+} ions experience a stronger crystal field in the oxide than in the fluoride crystal.

TABLE III. Observed and estimated positions of the spin-orbit components of the zero-phonon electronic energy levels in MgO:Ni^{2+} and associated Huang-Rhys parameter.

Excited levels (spin-orbit components)	Zero-phonon energy (cm^{-1})	S parameter
$^3T_2(^3F)E$	8 002	1.42
T_1	8 180	1.45
T_2	8 422	1.42
A_2	8 842	1.42
$^1E(^1D)$	~13 000	0.27
$^3T_1(^3F)\ A_1$	13 000±100	~3.22
T_1	13 500±100	~3.13
T_2	14 300±100	~3.13
E	14 750±100	~1.54
$^1T_2(^1D)$	21 100	1.81
$^3T_1(^3P)E$	23 895	3.48
T_2	24 040	3.22
T_1	24 200±100	~3.22
A_1	24 400±100	~3.13

Then the TS matrices can be solved for small variations δ (Dq) of the crystal-field parameter and the results used to determine the Huang-Rhys parameter S associated with each excited state[3,4]—this parameter determines the relative positions of the excited-state and ground-state potential curves in the single configuration coordinate diagrams (see Tables II and III).

Finally, we can use these data first to determine the $\hbar\omega$ phonon energies which lead, with the help of the line-shape functions W_p (S, $\hbar\omega$, T) defined in the theory of Struck and Fonger, to the best overall fit to the absorption and emission spectra and we find $\hbar\omega \simeq 250\ \mathrm{cm}^{-1}$ in the case of MgF_2:Ni^{2+} and $\hbar\omega \simeq 310\ \mathrm{cm}^{-1}$ in the case of MgO:Ni^{2+}. These values correlate well, for example, with the infrared fluorescence decay data reported in Sec. III. They allow us to reproduce the shapes and the widths of the bands almost perfectly. The most important deviations only occur in the case of the spin-forbidden transitions involving state $^1T_2(^1D)$; in that case, the calculated bandwidths are narrower than the observed ones. This discrepancy has to be attributed to coupling of state $^1T_2(^1D)$ to a phonon mode of different symmetry (see Sec. III).

In the same way, the single configuration coordinate diagrams can be used to calculate the S parameter associated with each of the excited-state absorption transitions and, by taking the same phonon frequencies as above, they can be used to calculate the corresponding W_p line-shape functions. Comparison of these results with the available experimental data—low-temperature ESE and room-temperature ESA as well as infrared emission spectra—is made in Fig. 11 in the case of MgO:Ni^{2+} and Fig. 12 in the case of MgF_2:Ni^{2+}. These figures allow us to conclude as follows.

(1) The most important failure of the single configuration coordinate model occurs in the case of the spin-forbidden ESA transition $^3T_2(^3F)\rightarrow{}^1T_2(^1D)$: a very sharp line is predicted where a band is observed. Nevertheless, this failure should not critically influence the predictions regarding laser performance—pumping efficiency, emission cross section, gain curve—since this ESA process has a very low cross section (see Sec. V).

(2) The model gives a much better agreement in the case of the spin-allowed ESA transitions which end on state $^3T_1(^3P)$. In the case of MgO:Ni^{2+} (Fig. 11) the width and the position of the low-temperature $^3T_2(^3F)\rightarrow{}^3T_1(^3P)$ ESE band are almost perfectly reproduced. Only the shoulder which appears on the high-energy side ($\sim 17\,000\ \mathrm{cm}^{-1}$) of the corresponding ESA band observed at room temperature is hard to interpret. In the case of MgF_2:Ni^{2+} the predictions appear less satisfactory; however, we remember that the calculations have been made on the basis of the only orbital components so that the agreement would be certainly better

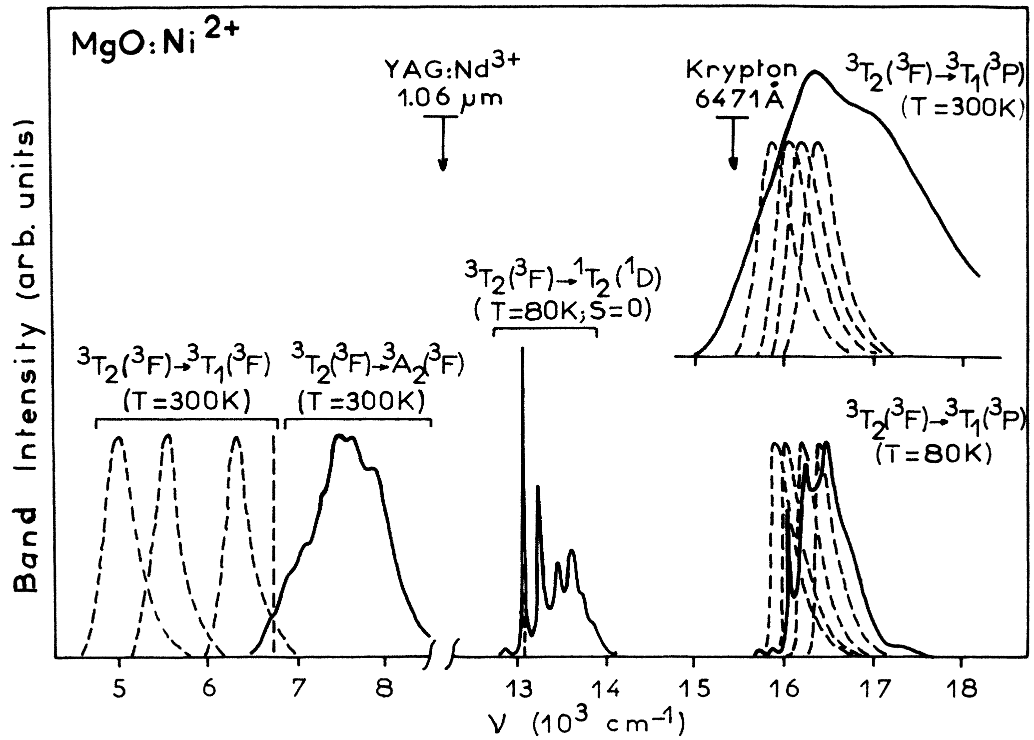

FIG. 11. Positions and band shapes of the ESA spectra obtained by using the CC model and the SF theory (— — —) compared with the available experimental data (——) such as infrared emission, ESE, and ESA in MgO:Ni^{2+}.

by including spin-orbit coupling.

(3) Because of the weak intensity of the probe beam and the poor sensitivity of the detectors at wavelengths longer than 1.6 μm, but also because of the experimental limitation arising from the spontaneous emission of the samples which overwhelms the halogen probe beam in the fluorescence region, no ESA signal could have been detected in the infrared domain. Thus, Figs. 11 and 12 only show a comparison between the wavelength domains spanned by the infrared emission, the one of interest for lasing action, and by the ${}^3T_2({}^3F)\rightarrow{}^3T_1({}^3F)$ excited state absorption, as it is predicted with the configuration

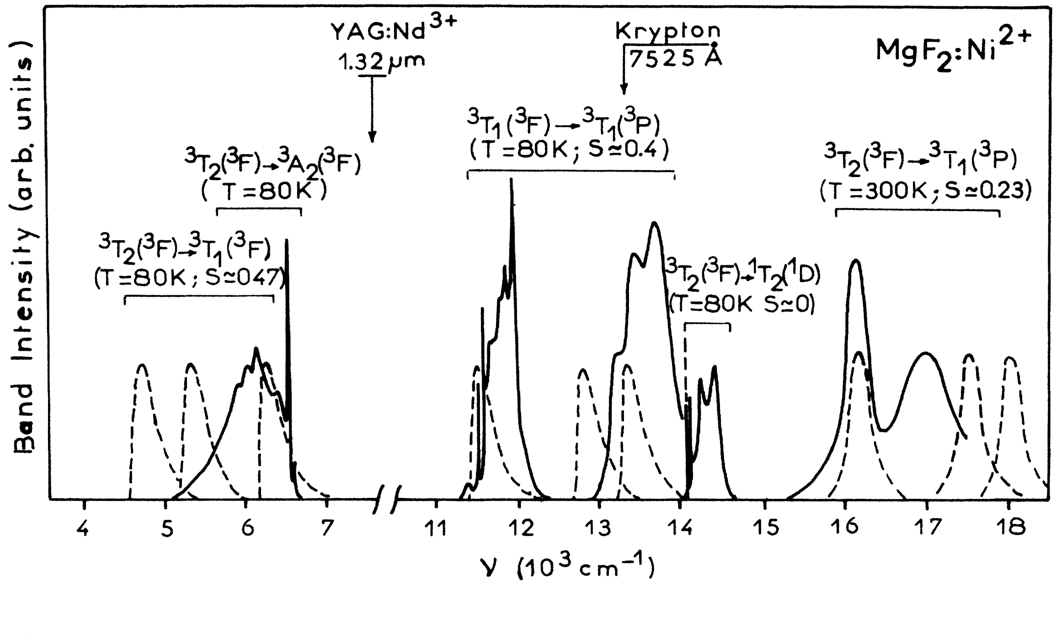

FIG. 12. Positions and band shapes of the ESA spectra obtained by using the CC model and the SF theory (— — —) compared with the available experimental data (——) such as infrared emission, ESE, and ESA in MgF_2:Ni^{2+}.

curves (CC) model. Though very approximate, this comparison allows us to make two interesting observations: (i) it looks clear that the lasing properties in MgO:Ni^{2+} will be less influenced by excited-state absorption than they will in MgF_2:Ni^{2+} and (ii) though infrared emission seems to be entirely overlapped by excited-state absorption in the case of MgF_2:Ni^{2+}, the ESA transitions to the two higher-lying orbital components of state $^3T_1(^3F)$ at about 5300 and 6100 cm^{-1} are sufficiently well separated to permit a useful gain cross section in the fluorescence region. This correlates well with the laser data which indicate a maximum wavelength tunability ranging from about 5500 cm^{-1} (~ 1.8 μm) to 6200 cm^{-1} (~ 1.6 μm).[19,20] Such a result, in turn, supposes excited-state absorptions [of type $^3T_2(^3F) \rightarrow {}^3T_1(^3F)$] and stimulated emissions having cross sections of the same order of magnitude, which we already noted in a previous article in the case of the V^{2+}- and Cr^{3+}-doped low-field systems.[4]

(4) Figures 11 and 12 also allow us to verify unambiguously that the most suitable pump wavelengths, for a good pump efficiency and a low laser threshold in each system, are at 1.06 μm in the case of MgO:Ni^{2+} and at 1.32 μm in the case of MgF_2:Ni^{2+} of a CW or pulsed YAG:Nd^{3+} laser. Pumping MgF_2:Ni^{2+} with a Krypton laser at 7525 Å, as we have done in the past,[17] should be avoided because of $^3T_1(^3F) \rightarrow {}^3T_1(^3P)$ excited-state absorption. On the other hand, pumping MgO:Ni^{2+} at low temperature with a Krypton laser at 6471 Å should lead to interesting lasing performance.

ACKNOWLEDGMENTS

Thanks are expressed to N. B. Manson, M. M. Abraham, and W. A. Sibley for providing us with the MgO:Ni^{2+} single crystals, and J. Y. Henry, F. Auzel, and B. Duviller for the MgF_2:Ni^{2+} samples. This work was supported in part by the French Direction des Recherches et Etudes Techniques (DRET) Grant No. 84/071. The Laboratoire de Physico-Chimie des Matériaux Luminescents is a "Unité Associeé No. 442 du Centre National de la Recherche Scientifique" (France).

---

[1] W. M. Fairbank, Jr., G. K. Klauminzer, and A. L. Schallow, Phys. Rev. B **11**, 60 (1975), and references therein.

[2] M. L. Shand and J. C. Walling, IEEE J. Quant. Electron. **QE-18**, 1152 (1982); M. L. Shand and H. P. Jenssen, *ibid.* **QE-19**, 480 (1983).

[3] L. J. Andrews, S. M. Hitelman, M. Kokta, and D. Gabbe, J. Chem. Phys. **84**, 5229 (1986).

[4] R. Moncorgé and T. Benyattou, preceding paper, Phys. Rev. B **37**, 9177 (1988).

[5] B. D. Bird, G. A. Osborne, and P. J. Stephens, Phys. Rev. B **5**, 1800 (1972).

[6] M. J. L. Sangster, G. Peckham, and D. M. Saunderson, J. Phys. C **3**, 1026 (1970).

[7] M. J. L. Sangster and C. W. McCombie, J. Phys. C **3**, 1948 (1970).

[8] N. B. Manson, Phys. Rev. B **4**, 2645 (1971); **2656** (1971).

[9] J. E. Ralph and M. G. Townsend, J. Chem. Phys. **48**, 149 (1968); J. Phys. C **3**, 8 (1970).

[10] W. E. Vehse, K. H. Lee, S. I. Yun, and W. A. Sibley, J. Lumin. **10**, 149 (1975).

[11] M. V. Iverson, J. C. Windscheif, and W. A. Sibley, Appl. Phys. Lett. **36**, 183 (1980).

[12] M. D. Sturge, J. Phys. C **20**, 91 (1967).

[13] N. Moreau, A. C. Boccara, and J. Badoz, Phys. Rev. B **10**, 64 (1974).

[14] J. Ferguson, H. J. Guggenheim, H. Kamimura, and Y. Tanabe, J. Chem. Phys. **42**, 775 (1965).

[15] J. M. Breteau, Ph.D. thesis, University of Paris, 1986.

[16] L. N. Feuerhelm and W. A. Sibley, J. Phys. C **16**, 799 (1983).

[17] R. Moncorgé, F. Auzel, and J. M. Breteau, Philos. Mag. B **51**, 489 (1985).

[18] L. F. Johnson, H. J. Guggenheim, and R. A. Thomas, Phys. Rev. **149**, 179 (1966).

[19] P. F. Moulton and A. Mooradian, Appl. Phys. Lett. **35**, 838 (1979).

[20] A. Mooradian, Laser Focus **15**, 28 (1979).

[21] P. F. Moulton, *Handbook of Laser Science and Technology* I, *Lasers and Masers,* edited by M. J. Weber (Chemical Rubber Company, Boca Raton, 1982), p. 60.